© Indian Academy of Sciences

Correlating the microstructural and optical properties of vanadium ion-doped ZnO nanocrystals

**SHASHANK KINRA[1], MRITUNJOY PRASAD GHOSH[2], SIPUN MOHANTY[2],
RAVI KANT CHOUBEY[1] and SAMRAT MUKHERJEE[2,*]**

[1] Department of Applied Physics, Amity Institute of Applied Sciences, Amity University, Noida 201313, India
[2] Department of Physics, National Institute of Technology Patna, Patna 800005, India
*Author for correspondence (samrat.udc@gmail.com)

Abstract. This article deals with the synthesis, structural and optical characterizations of vanadium ion-doped ZnO nanoparticles. Four nanosized samples with a generic composition $Zn_{1-x}V_xO$ ($x = 0.00, 0.02, 0.04$ and 0.06) were prepared using standard co-precipitation method. X-ray diffraction studies confirmed the existence of hexagonal wurtzite crystal structure and phase purity of prepared samples. Mean crystallites size within the range of 25 ± 3 nm was obtained from Scherrer's formula. The compressive microstrain in the pure ZnO sample as obtained from Williamson–Hall plot ensured the presence of vacancies inside the nanocrystals. The surface morphology of doped ZnO nanocrystals was studied using field-emission scanning electron microscope image. Undoped ZnO nanoparticles showed a strong optical absorption near 390 nm. A redshift in direct bandgaps with increasing vanadium ions in ZnO matrix was noticed. Vanadium ions were present in three different oxidation states ($+2, +3$ and $+4$) within the host ZnO structure as obtained from X-ray photoelectron spectra. Photoluminescence studies also detected the existence of both zinc and oxygen vacancies in the synthesized nanoparticles.

Keywords. ZnO nanoparticles; Williamson–Hall plots; optical bandgap; X-ray photoelectron spectroscopy; oxygen vacancies.

1. Introduction

In the past few decades, a substantial amount of investigations in respect to transitional metal (TM)-doped oxide-based semiconductors were conducted to explore the modifications triggered in several physical properties of such semiconductor materials by the dopant ions [1–3]. Further, the occupancy of TM ions in the cationic or interstitial sites in the host lattice was observed to greatly affect the electronic properties of the resultant semiconductor, which led to the research development in different fields such as light-emitting devices, quantum computers and spin field-effect transistors [4].

From the past decade, many investigations in respect to zinc oxide, a prominent member II–VI compound, semiconductors have been conducted in the field of the photovoltaic, solar cell, photocatalyst, dye-degradation, gas sensor, photonics, thin-film transistors, etc., [5–8] attributed to its distinctive properties like wide bandgap (3.37 eV), large exciton binding energy (60 meV) and superior chemical stability [9–11]. Adding to this, the observation of magnetic properties in ZnO doped with TMs has invoked a new interest all over the world in recent years [12,13]. Because of the direct bandgap of ZnO compound, this

material is self-sufficient to produce light in response to optical excitation. Therefore, an electro-optical coupling is possible in this system and proper tuning of electro-optical coupling may revolutionize the electro-optical field [14,15]. It has been found that vanadium doping can lead to defect formation during synthesis. Versatile magnetic ordering has been achieved by the substitution of vanadium in the host lattice of zinc oxide due to the presence of multivalent vanadium ion [16–18]. It can also be noted that the ionic radii of vanadium are smaller than zinc, which can allow the band engineering to utilize vanadium (V)-doped zinc oxide nanostructure in sensing applications. Further, vanadium is known to exhibit properties scalable for sensing and memory device applications. To realize such possibilities many theoretical and experimental research has been carried out in recent years. In 2009, Tahir *et al* [19] observed a blue shift in the bandgap of V-doped ZnO with the increase in doping concentration of vanadium. The ferroelectric response in two dimensional V-doped ZnO was observed by Gupta *et al* in 2013 [20]. Ftouhi *et al* [21] observed an enhancement in the transparency of the ZnO–V-based films in the visible region with the increase of doping concentration. However, a conflicting result was brought to light by Kawashima *et al* [22] in the year 2017, they observed a

decrease in both the bandgap as well as transparency by increasing doping of vanadium ions using RF magnetron sputtering. A similar result was obtained by El Ghoul [23] using sol–gel method [23]. Thus, an inconsistency is apparent in the reports relative to the interpretation of the origin and nature of magnetic behaviour in magnetic ion-doped semiconductors. For the development of spin-based device applications, it is necessary to realize the ion inter-actions evolving in the system for which experimental investigation of the electronic structure of V-doped ZnO nanoparticles is crucial. Vanadium ions can exist in multiple oxidation states in the host matrix. Doping of V ions in place of Zn^{2+} ions in ZnO matrix may increase the electron cloud density for charge neutrality. It is expected that the substitution of V ions may improve the electronic properties and tune the bandgap of ZnO nanoparticles. Vanadium ion-doped nanosized ZnO with enhanced physical properties will help researchers to explore its use in optoelectronics and sensor application fields [24–26].

In this study, we report the microstructural and optical properties of $Zn_{1-x}V_xO$ (x = 0.00, 0.02, 0.04, 0.06) nanoparticles at room temperature, synthesized using standard co-precipitation route. A clear signature of tailored semiconducting behaviour at room temperature in nano-sized ZnO samples with the doping of vanadium ions was observed. Suitable correlations between the microstructural and optical properties of vanadium ion-doped ZnO nanocrystals have been formulated in this study.

2. Experimental

The bottom-up chemical co-precipitation technique has been used to synthesize the vanadium-doped zinc oxide [$Zn_{1-x}V_xO$: x = 0.00, 0.02, 0.04, and 0.06] nanocrystals [27–29]. The following chemicals VCl_3, PVP and $ZnCl_2$ were utilized for fabricating the V-doped ZnO nanoparticles without further purification. The measured amount of the above chemicals depending on the stoichiometric ratio were first dissolved in 200 ml de-ionized water under steady stirring of 700 rpm. To attain a pH value of 11, an aqueous NaOH solution was then put dropwise into the solution under the same stirring condition. This resulted in the formation of a grey colour precipitate. Further, for 2 h, the solution so obtained containing the precipitate was digested at 80°C under the same stirring condition, resulting in the completion of all chemical reactions. In the next step, numerous washes of the precipitate using de-ionized water were carried out. The washing process was repeated with ethanol until the pH value attained 7. The precipitate was then left to dry off in room atmosphere. This was followed by grounding the resultant into powder. In the next step, calcination of the obtained powder was carried out in a furnace at 400°C for 4 h with a constant heating rate of 4°C min^{-1}, which was then cooled down slowly. The samples of synthesized nanopowder have been designated with specific

indices, i.e., V-00, V-02, V-04 and V-06, respectively, with an increase in the vanadium ions concentration. All the physical characterizations have been carried out on these nanopowder samples.

The structural analysis of the prepared powder samples has been accomplished using powder X-ray diffractometry followed by a Rietveld refinement. X-ray diffractometer (Bruker D8-Advance) with K_α characteristic line of copper source (λ = 1.5406 Å) has been utilized in obtaining the powder diffraction patterns of all samples at room temperature. Diffraction data have been recorded within a range of $20^\circ \leq 2\theta \leq 80^\circ$ at a fixed scan rate of 0.02° s^{-1}. Both the surface morphology and chemical composition of the V-doped ZnO nanocrystals were analysed using field-emission scanning electron microscope (FESEM) micro-scopy (FESEM, JEOL-JSM 5600) and energy-dispersive X-ray spectroscopy (EDS) at 300 K. X-ray photoelectron spectroscopy (XPS) measurements were carried out using PHI-5702 system with Al K_α radiation. In optical studies, ultraviolet-visible spectroscopy (UV–Vis) has been carried out followed by photoluminescence (PL). Absorption spectra of all vanadium ion-doped ZnO samples were taken within 200 to 900 nm at room temperature using UV–Vis spectrophotometer (Hitachi, U-3010). Photoluminescence (PL) spectra of all the samples were recorded at 300 K using Perkin-Elmer fluorescence spectrometer.

3. Results and discussion

3.1 *Structural studies*

The crystalline nature of the synthesized vanadium-doped zinc oxide ($V_xZn_{1-x}O$: x = 0.00, 0.02, 0.04 and 0.06) samples was confirmed through the X-ray diffraction (XRD) plots, which are depicted in figure 1. The obtained diffraction pattern confirmed the formation of a single-phase hexagonal structure with a space group of P6$_3$mc, as the pattern shared an excellent match with the ICDD card number 01-079-0207. The pattern exhibited all the characteristic peaks (100), (002), (101), (102), (110), (103), (200), (112), (201), (004) and (202) confirming the formation of single-phase wurtzite-structured zinc oxide [27]. The absence of arbitrary peaks further eliminated the possibility of the formation of any undesired crystallographic phases. General structure analysis system (GSAS) with EXPUGI interface [27,28] was used for the Rietveld refinement of diffraction profile. Pseudo–Voigt function along with Finger-Cox-Jephcoat asymmetry function was used for the fitting of diffraction profiles and for correcting the axial divergence. All information corresponding to lattice parameters and refinement parameters that included good-ness of fit (χ^2) and reliability factors (R_p, R_{wp}, R_F^2) are compiled in table 1. It is important to note that in the case of nanocrystalline materials generally the values of reliability factors are found to be high in comparison to the bulk
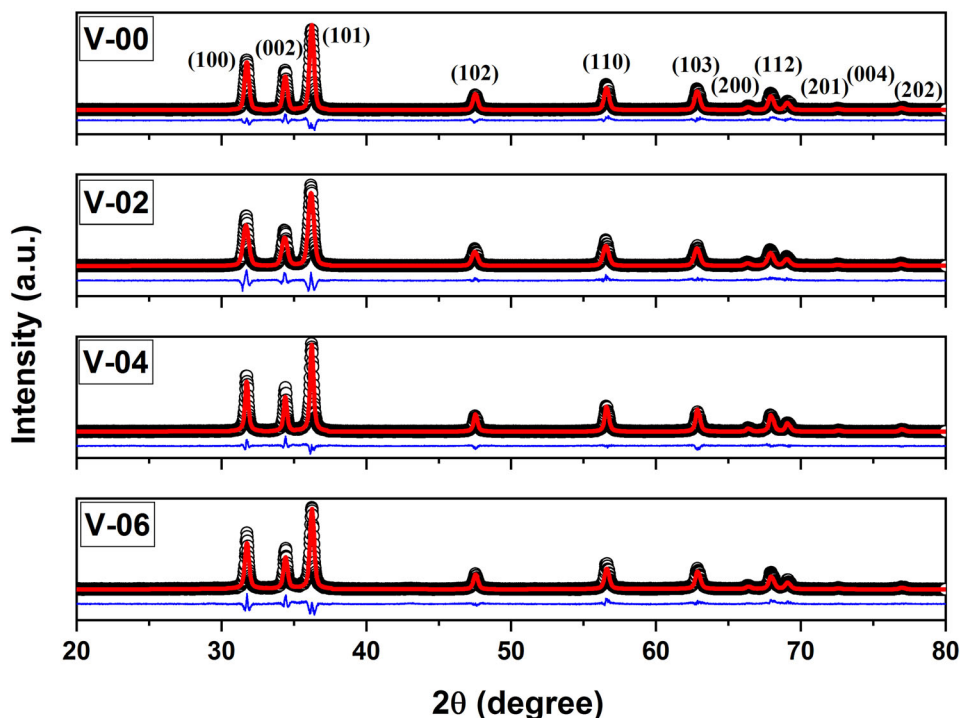
Figure 1. Room temperature XRD patterns of all the samples.

Table 1. Unit cell parameters and refinement factors of all the samples.

Sample Id	V-00	V-02	V-04	V-06
Space group	P63mc	P63mc	P63mc	P63mc
Cell parameters				
a (Å)	3.2504	3.2498	3.2509	3.2505
c (Å)	5.2062	5.2041	5.2069	5.2064
c/a	1.6017	1.6013	1.6016	1.6017
U	0.3793	0.3800	0.3795	0.3793
Volume (Å^3)	47.654	47.596	47.657	47.641
Refinement factors				
R_{wp} (%)	9.28	8.98	9.46	9.63
R_p (%)	8.92	9.52	9.45	9.74
R_f^2 (%)	3.97	4.67	5.19	6.35
χ^2	2.46	2.39	2.61	2.91

materials [29,30]. However, the obtained value of goodness of fit (χ^2) was less than 3. It implied a good match between the simulated data and raw data; therefore, justified the merit of refinement. The value of the lattice parameter for undoped zinc oxide so obtained is higher than the reported values of its bulk counterpart (a = 3.2495 Å, c = 5.2069 Å) [27,31]. Such aberration can be attributed to the size effects of intrinsic defects such as zinc interstitials (Zn_i) and oxygen vacancy (V_o) in nanoscale. Further, it is to be noted that vanadium is a multivalent TM that can exist in different valence states of +2, +3, +4 and +5, respectively. The ionic size of vanadium at a higher valence state is

comparatively lesser than that of zinc (Zn^{2+}) ions [29,32]. This triggers the contraction of the lattice. Furthermore, the method of preparation, processing temperature can also induce effects leading to lattice parameter increment. Determination of lattice parameters is performed by using the relation [27,33]

$$\frac{1}{d^2} = \frac{4}{3}\left(\frac{h^2 + hk + k^2}{a^2}\right) + \frac{l^2}{c^2}. \tag{1}$$

The following section discusses the particle size and intrinsic strain calculation through a comparison drawn between three well-known methods of calculation.

Scherrer's method: Broadening of XRD profiles in nanocrystals generally appears as a consequence of crystalline effect, intrinsic strain effect and instrumental effects. The broadening part further involves instrumental and physical broadening [28,34], from which correction of instrumental broadening uses the relation,

$$\beta_d^2 = \beta_m^2 - \beta_i^2, \tag{2}$$

where β_m denotes the measured broadening and (β_i, β_d) represents the instrumental and corrected broadening. Here, the position calibration and calculation of instrumental broadening were done using LaB_6 as standard reference material. The average crystallite size is obtained by using the Scherrer equation [33], as follows:

$$\langle D \rangle = 0.89\frac{\lambda}{\beta_d \cos\theta}, \tag{3}$$

where λ signifies the wavelength of K_α line (1.5406 Å) of copper source, D represents the mean particle size and β_d is the full-width at half-maximum of characteristic (101) peak. Obtained values of mean crystallite size are listed in table 2a.

Williamson–Hall plot: The mean crystallite size obtained from the Scherrer formula also contains the effect of peak broadening due to the existence of intrinsic microstrain inside the nanocrystals. Strain develops in a tiny crystal due to the presence of multiple defects like point defects, planar defects and grain boundaries [28]. Williamson–Hall (W–H) method normally takes these contributions into an account to provide comparatively accurate average crystallite size. According to W–H method, physical line broadening results from the size of nanocrystals and the microstrain present in them. Therefore, the total broadening is represented as [34]

$$\beta_{total} = \beta_{size} + \beta_{strain}. \tag{4}$$

In this study, uniform deformation model has been used to calculate the average particle size and microstrain by applying W–H equation. This model considers strain to be isotropic in nature [35], i.e., uniform strain throughout the crystallographic direction appearing due to crystal imperfections. The peak broadening due to strain is shown by the relation

$$\beta_{strain} = 4\varepsilon \tan\theta. \tag{5}$$

The total broadening is then given by the following relation [28,34]

$$\beta_{hkl} \cos\theta = \frac{k\lambda}{D} + 4\varepsilon \sin\theta. \tag{6}$$

Figure 2 shows the W–H plot of all the synthesized samples. The plot between the $\beta_{hkl}.\cos\theta$ (*Y*-axis) and $4\sin\theta$ (*X*-axis) facilitates the evaluation of intrinsic strain and average particle size through the values obtained from slope and intercept. Estimated values of crystallite size and microstrain are shown in table 2b.

Halder–Wagner method: In the method discussed above, the XRD profiles are generally assumed as Lorentzian function and the broadening as Gaussian function or vice-versa. As the observed diffraction peaks are not purely Gaussian or Lorentzian, a Pseudo–Voigt function which is a convolution of both Lorentzian and Gaussian function is normally used to shape all the diffracted peaks. The upper region of the diffracted peak matches efficiently with the Gaussian function, whereas the tail region fails to match well and a vice-versa situation is noticed with the Lorentzian function [36,37].

In the Halder–Wagner (H–W) method, the overall peak broadening is assumed to be best fitted with a symmetric Voigt function [36]. This method usually takes more precedence from the peaks present in the region of lower and middle angles, where less amount of overlapping occurs among the diffracted peaks.

The H–W method illustrates the correlation between the lattice strain and the size of crystallites as [27]:

$$\left(\frac{\beta}{\tan\theta}\right)^2 = \frac{k\lambda}{D}\frac{\beta}{\tan\theta\sin\theta} + 16\varepsilon^2. \tag{7}$$

Figure 3 depicts the H–W plot of the entire samples. The plot of $\left(\frac{\beta}{\tan\theta}\right)^2$ with respect to $\frac{\beta}{\tan\theta\sin\theta}$ takes a straight-line form, whose slope gives the mean crystallite size and intercept yields the developed microstrain in nanocrystals. Obtained values of both crystallite size and microstrain are listed in table 2c.

3.2 FESEM image analysis

FESEM image of V-04 sample together with EDS pattern is shown in figure 4. Vanadium ion-doped ZnO nanocrystals

Table 2. Average crystallite size and intrinsic strain calculated using Scherrer's method, Williamson–Hall plot and Halder–Wagner plot.

| (a) **Using Scherrer method**				
Sample ID	V-00	V-02	V-04	V-06
Space Group	P63mc	P63mc	P63mc	P63mc
Crystallite size (nm)	25	22	28	27
(b) **Using Williamson–Hall plot**				
Sample ID	V-00	V-02	V-04	V-06
Space group	P63mc	P63mc	P63mc	P63mc
Crystallite size (nm)	23	19	25	24
Strain ($\times 10^{-3}$)	–0.572	–1.771	–0.336	–0.364
(c) **Using Halder–Wagner plot**				
Sample ID	V-00	V-02	V-04	V-06
Space Group	P63mc	P63mc	P63mc	P63mc
Crystallite size (nm)	23	21	26	24
Strain ($\times 10^{-3}$)	–0.893	–1.457	--.673	–0.721
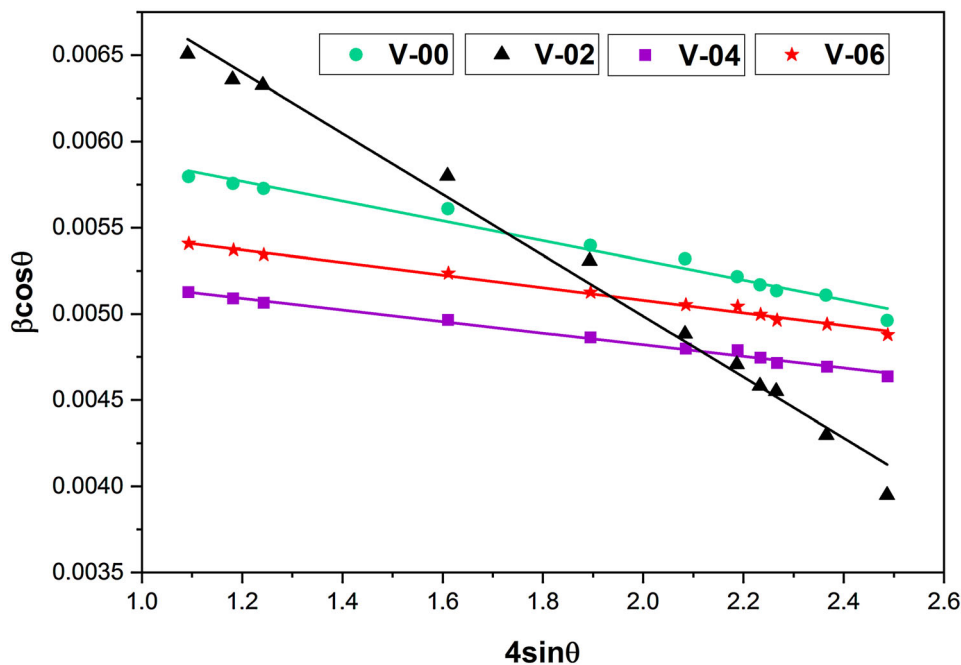
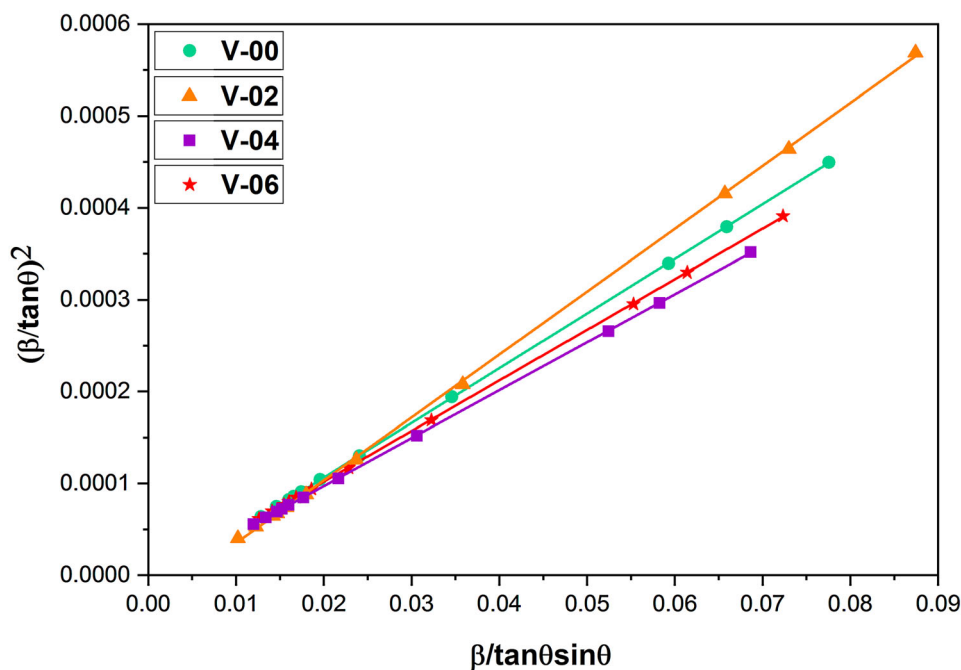**Figure 2.** Williamson–Hall (W–H) plots of all the samples.

Figure 3. Halder–Wagner (H–W) plots of all the samples.

with good uniformity in both size and shape was achieved through wet chemical route, which is also verified by FESEM image. An average grain size of 29 ± 1 nm was obtained from the histogram (in inset) for V-04 sample, which was consistent with XRD results. The EDS spectra traced the existence of Zn, V and O elements, respectively, in the host compound. The weight percentage of V ions in V-04 sample was found to be 3.27%, which was almost in

accordance with the taken value during synthesis. No foreign elements were detected in the EDS pattern [28,33].

3.3 *X-ray photoelectron spectra studies*

As the vanadium ion exists in multiple oxidation states, determination of oxidation states of such ions becomes
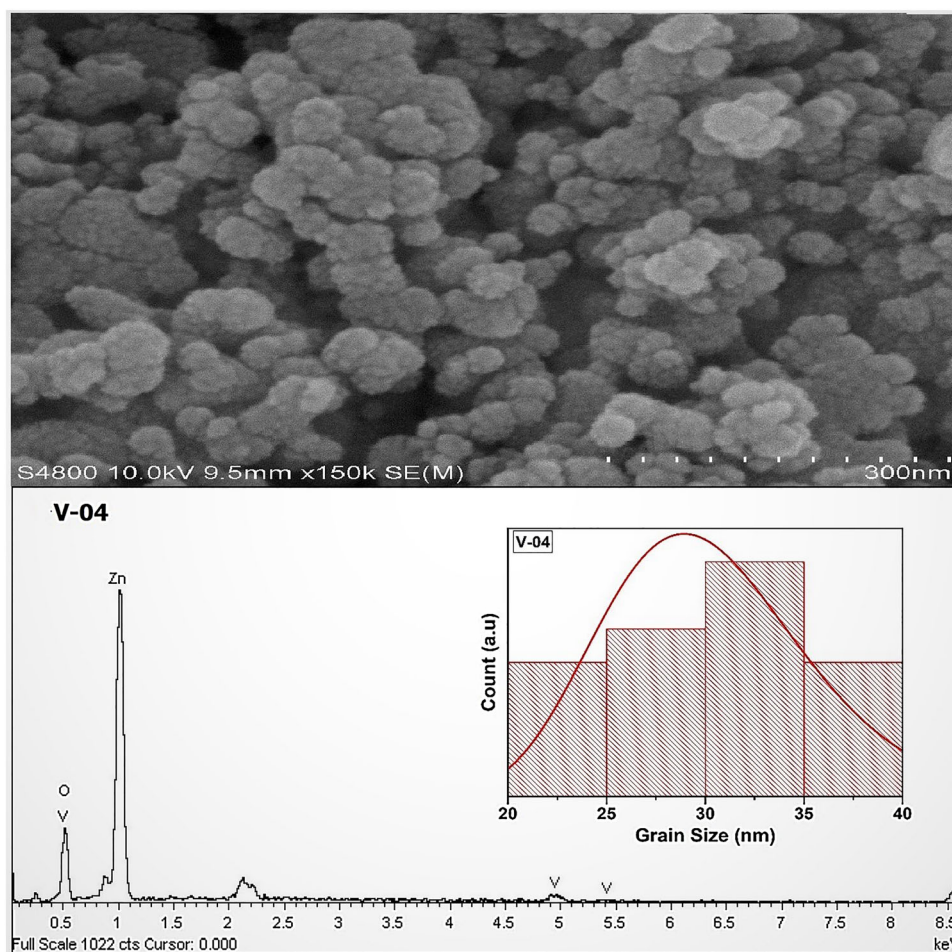
Figure 4.   FESEM image with EDS of V-04 sample.

essential inside the hexagonal ZnO matrix to explain the modified physical properties. The oxidation state of vanadium ions within ZnO nanocrystals was estimated using X-ray photoelectron spectra. The deconvoluted XPS spectrum of vanadium 2p energy level for V-06 sample is depicted in figure 5. Pseudo–Voigt function was applied to get the best fitting of $2p_{3/2}$ and $2p_{1/2}$ peaks. Normally vanadium in pure metallic form displays the binding energy of both $2p_{3/2}$ and $2p_{1/2}$ energy levels near 512.3 and 519.7 eV, respectively [29]. Observed increase in the binding energy of these two ($2p_{3/2}$ and $2p_{1/2}$) energy states, when compared with the pure vanadium metal, confirmed the existence of vanadium ions in higher oxidation states in ZnO matrix. The deconvoluted XPS spectrum verified the presence of vanadium ions in +4, +3 and +2 oxidation states within the host crystal structure, respectively. The binding energy of electrons in 2p states is comparatively larger for V (IV) ions with respect to both V (II) and V (III) ions due to the presence of less unpaired valence electrons [38]. The binding energy of $2p_{3/2}$ and $2p_{1/2}$ energy levels of V (II), V (III) and V (IV) ions in the host ZnO structure for V-06 sample is given in table 3. Silversmit *et al* [39] investigated the V (2p) binding energies in different

vanadium oxides and also reported the binding energies for V (II), V (III) and V (IV) energy states. Our results were found in close agreement with those findings. The proportion of V^{4+} ions in the host ZnO matrix is larger in comparison to other V ions as verified by XPS data analysis.

3.4 *Absorption spectra studies*

In nanodomain, the physical properties of materials are entirely modified by the dimension of that specific material. Especially for semiconducting nanoparticles, it is observed that size plays a crucial role while exploring several properties. The absorption properties of nanomaterials are usually explored by the UV–vis spectroscopy. In this study, UV–vis spectra of all the vanadium-doped nanosized ZnO samples were taken at room temperature within the range of 200 to 900 nm, respectively. Estimation of optical bandgap together with the effect of size and variation of vanadium ions in host ZnO was the primary aim of this study. As we already know that bulk ZnO manifests direct optical band transition with a direct bandgap near 3.3 eV at 300 K [27,40]. In this regard, Tauc plot is extensively used to
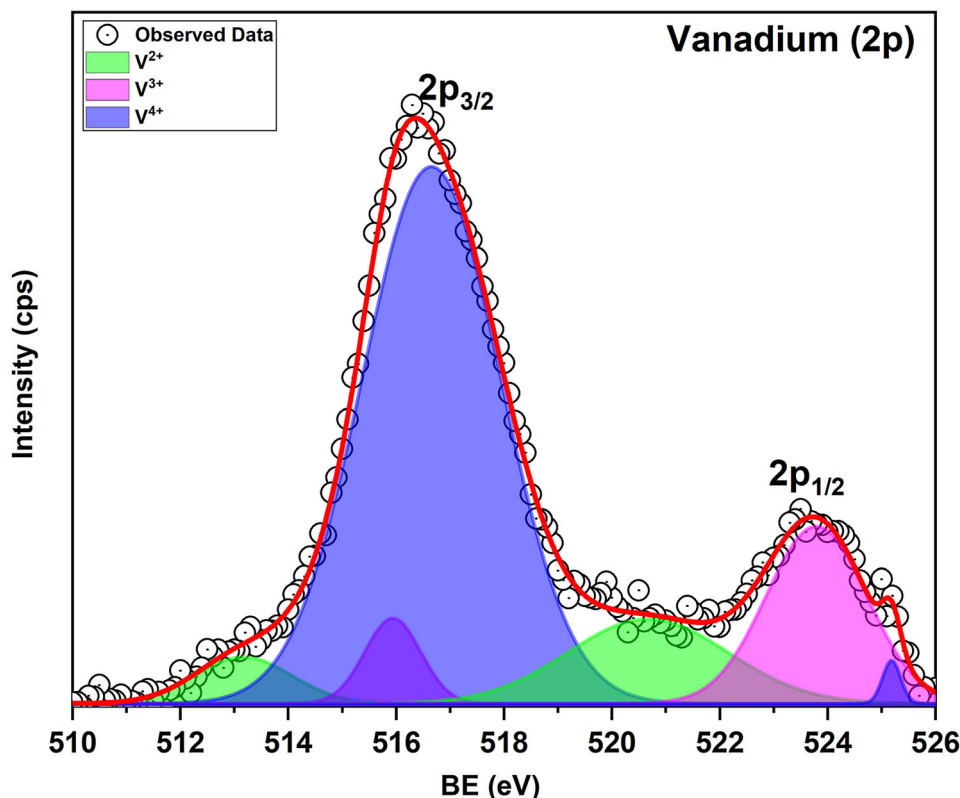
Figure 5. Fitted XPS spectra of V-06 sample recorded at room temperature.

Table 3. Data obtained from fitted XPS spectra.

Oxidation state	$2p_{1/2}$ (eV)	$2p_{3/2}$ (eV)	($2p_{1/2}$ - $2p_{3/2}$) splitting (eV)
V (II)	520.6	513.1	7.5
V (III)	523.7	515.9	7.8
V (IV)	525.1	516.6	8.5

evaluate the optical bandgap of semiconducting materials. We have used the Tauc plot to estimate the direct optical bandgap of all the vanadium-doped nanometre-sized ZnO samples. The following stated Tauc relation has been applied [41]

$$\alpha(v)hv = C\left(hv - E_g\right)^n, \tag{8}$$

where α denotes the absorption coefficient of a semiconducting compound, hv shows the photon energy, C is a proportionality constant, E_g signifies the optical bandgap and n symbolizes an exponent. Generally, the values of n determine the type of optical transition between the valance band and conduction band (CB). In the case of direct bandgap semiconducting material, the exponent attains a value of 0.5 while it takes a value of 2 for indirect band transition. Estimation of absorption coefficient (α) for entire

prepared samples was performed by using the following relations [27,41]:

$$I = I_0 e^{-\alpha t} \text{ and } A = \log\left(\frac{I_0}{I}\right), \tag{9}$$

where A denotes the absorbance and t is the width of the cuvette containing the sample. Obeying equation (9), the absorption coefficient (α) may be written down as [27]

$$\alpha = 2.303\left(\frac{A}{t}\right). \tag{10}$$

For calculating the direct optical bandgap (E_g) of entire doped and undoped ZnO samples, a graph between $(\alpha hv)^2$ and hv is drawn, which is familiar as Tauc plot [27,29]. Figure 6 depicts the Tauc plots of all vanadium ion-doped ZnO nanoparticles. The undoped ZnO sample exhibited a
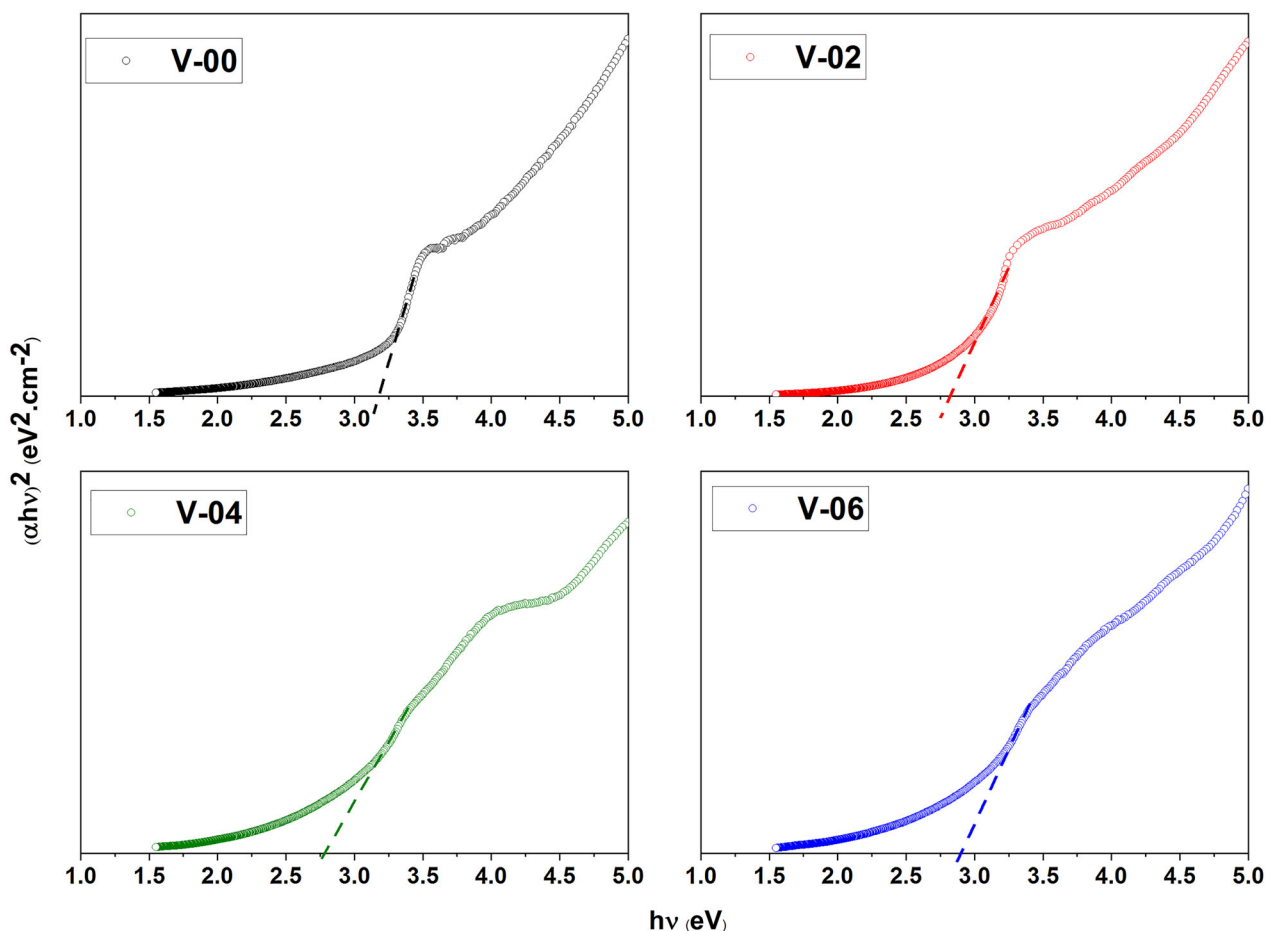
Figure 6.   Tauc plots of $Zn_{1-x}V_xO$ (x = 0.00, 0.02, 0.04 and 0.06) nanoparticles measured at 300 K.

strong optical absorption near 390 nm. Obtained values of E_g are 3.18 eV (V-00), 2.81 eV (V-02), 2.79 eV (V-04) and 2.89 eV (V-06), respectively, as per increasing vanadium dopant in host ZnO nanoparticles [27]. Sharp transition in pure ZnO sample indicated the monodispersed nature of nanoparticles. An increment in the mean diameter of nanoparticles with the increase of vanadium concentration resulted in a redshift of the bandgap. It is established that with the increase of the average diameter of nanoparticles, the overlap between atomic orbitals starts to increase, which results in the reduction of the bandgap. All the as-synthe-sized ZnO samples showed strong absorption in between 390 and 440 nm. These nanopowders are capable to absorb easily the violet and blue regions of the electromagnetic spectrum. As per the studies on absorption spectra of $Zn_{1-x}V_xO$ nanoparticles, it is obvious that these nanosized ZnO powders are the ideal candidate to cut off the violet and blue bands of electromagnetic spectrum [41].

3.5   *Photoluminescence studies*

Photoluminescence (PL) spectroscopy technique was used to determine and study the presence of defect levels

existing in the forbidden energy gap of the synthesized ZnO particles. Solutions of the synthesized nanoparticles were first excited by a Xenon laser light of the wavelength of 280 nm, and then scanned within the wavelength range of 350 to 600 nm at 300 K. Figure 7 represents the room temperature PL emission spectra of vanadium ions sub-stituted ZnO nanoparticles having different vanadium concentrations, i.e., 0% 2, 4 and 6%, respectively. A Gaussian function was used in the fitting of results obtained from the de-convoluted seven peaks present in the visible region along with the peak present in the UV region. In the fitted PL spectra of the prepared samples, a weak peak in the UV region is observed around 350 nm followed by a band of peaks in the visible region of 380 to 600 nm. The visible band consists of violet peaks ranging from 395 to 435 nm, blue peaks in the range of 468 to 493 nm, green peaks in the range of 517 to 566 nm, and yellow peaks ranging from 575 to 585 nm [33].

The presence of deep-level emission centres and/or non-radiative recombination centres affect the UV emis-sion intensity, which might have been the cause of the observed degradation. The UV peak observed at 354, 354 and 342 nm for the corresponding V-02, V-04 and V-06 samples appeared at a lower wavelength; i.e., blue shifted
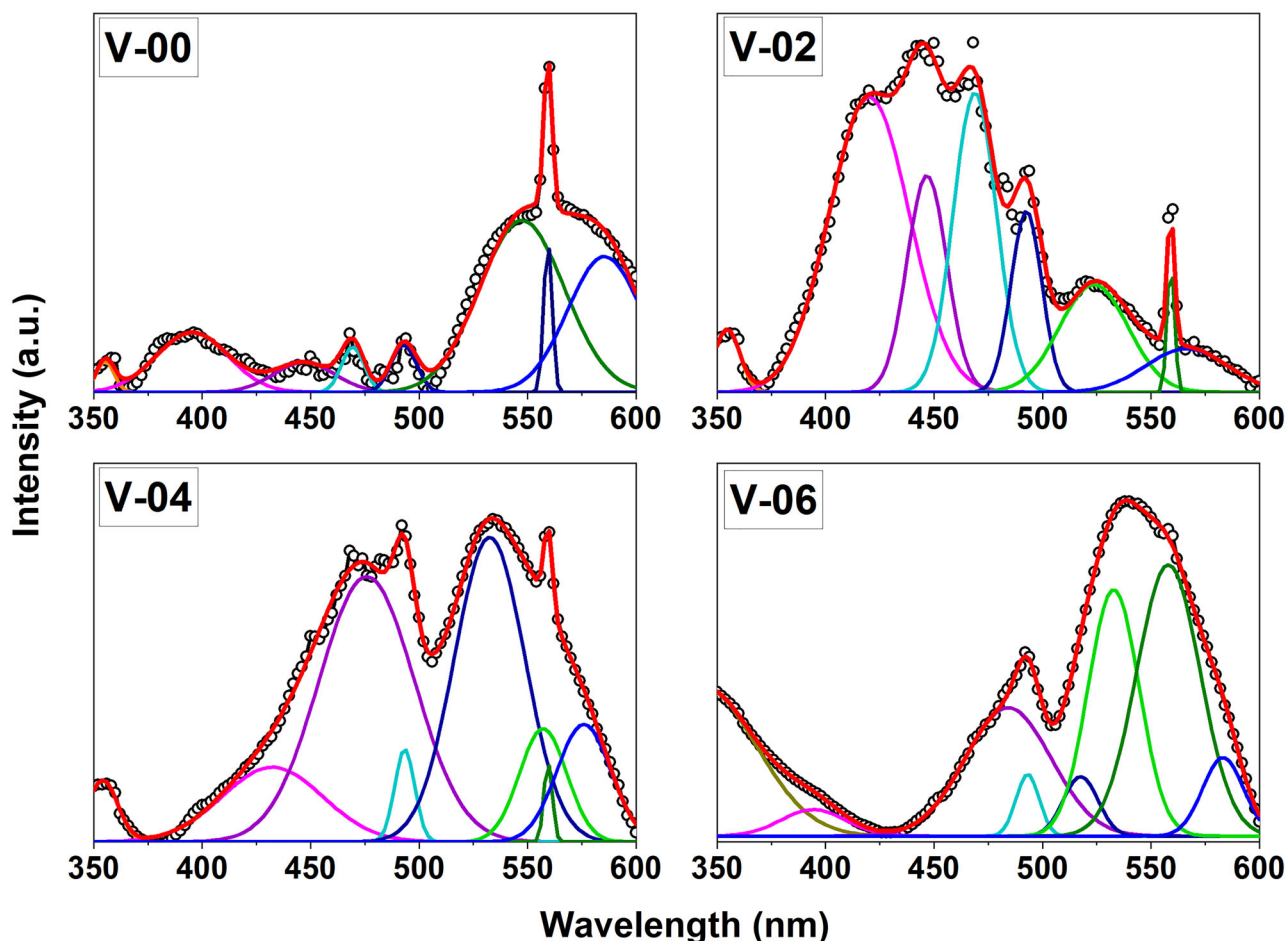
Figure 7. PL spectra obtained at room temperature for all the samples.

with respect to that of bulk ZnO (V-00) sample, observed at 355 nm. The origin of this peak is attributed to the point defects (interstitials, vacancies and anti-sites) particularly to their donor and/or acceptor levels which are generated in the forbidden energy gap of the band structure by such dopants/extrinsic defects in the system [33,42]. It can also be attributed to the presence of extrinsic impurities.

Violet emission peaks at 394 and 395 nm might have occurred due to the transition of the CB electrons to the acceptor energy levels of singly ionized oxygen vacancies (V_o^+) present near the valence band (VB). These vacancies trap holes which then behave as quasi-free holes and acquire low binding energy. Trapped electrons transitioning from zinc interstitials (Zn_i) to the VB might also have been the reason for the violet emission observable at 420 nm [43–47]. Trapped electron transitions from the singly ionized zinc interstitials (Zn_i^+) to the VB might attribute to the presence of violet emission at 432 nm. The violet emission peaks at 446 and 447 nm might have resulted from the recombination of trapped electrons in the doubly ionized zinc vacancies (V_{Zn}^{2-}) with the holes in the VB. Further, the

energy levels corresponding to the zinc interstitials (Zn_i), singly ionized zinc interstitials (Zn_i^+) and doubly ionized zinc vacancies (V_{Zn}^{2-}) which behave as shallow donor point defects, lie below the CB [42] resulting in quasi-free electrons having low binding energies trapped in such behaving point defects.

The blue emissions at 468, 469 and 475 nm might have resulted from the radiative recombination occurring in the electrons belonging to the CB with an oxygen anti-site (O_{Zn}), which behaves as an acceptor point defect whose energy level lies above (0.80 eV) the VB [42]. While the blue peak at 484, 492 and 493 nm may have resulted in the ramification of electrons of CB or the electrons which are trapped near the CB recombining with trapped holes of neutral oxygen vacancies (V_o) [48,49]. The green emission observed in the samples ranging from 517 to 559 nm can be attributed to the oxygen deficiency, such as the presence of single ionized oxygen vacancy (V_o^+) [50], the existence of oxygen anti-site [51], presence of V_o^{2+} centre [52] and the presence of zinc vacancy (V_{Zn}) [53]. While, yellow emissions at 575, 583 and 585 nm are the outcomes of interstitial oxygen defects (O_i) [50].

4. Conclusion

In this study, a correlation between microstructural and optical properties of vanadium ion-substituted zinc oxide nanoparticles was established. Four samples with varying vanadium percentage in host ZnO matrix [$Zn_{1-x}V_xO$: $x = 0.00, 0.02, 0.04$ and 0.06] were successfully obtained by using standard soft co-precipitation route. X-ray powder diffractograms ensured that the synthesized nanopowder samples contained pure hexagonal wurtzite crystallographic structure. Average crystallite sizes were estimated within 25 ± 3 nm from Scherrer's formula. A correlation among Scherrer's method, Williamson–Hall method and Halder–Wagner Method was established in connection to the crystallite size and microstrain, respectively. The mean crystallite size of synthesized samples obtained using all these methods was below 28 nm and also ensured that the samples were in nanodomain. The existence of notable microstrain was noticed in synthesized ZnO samples. The observed redshift in the optical bandgap is attributed to the increment in the mean diameter of nanoparticles. XPS studies revealed that vanadium ions existed in three different oxidation states inside the parent ZnO matrix. All the prepared ZnO samples containing nanoparticles showed strong absorption in between 390 and 440 nm. Careful analysis of PL spectra confirmed the presence of both Zn vacancies as well as oxygen vacancies in the samples, respectively.

References

[1] Zhang F, Cui H and Zhang W 2015 *Vacuum* **119** 131

[2] Ahmed S 2017 *Results Phys.* **7** 604

[3] Kafle B, Acharya S, Thapa S and Poudel S 2016 *Ceram. Int.* **42** 1133

[4] Fabbiyola S, JohnKennedya L, Ratnaji T, Vijaya J J, Aruldoss U and Bououdin M 2016 *Ceram. Int.* **42** 1588

[5] Andrade G R S, Nascimento C C, Silva Júnior E C, Mendes D T S L and Gimenez I F 2017 *J. Alloys Compd.* **710** 557

[6] Ariyakkani P, Suganya L and Sundaresan B 2017 *J. Alloys Compd.* **695** 3467

[7] Gwozdz K, Placzek-Popko E, Zielony E, Paradowska K M, Pietruszka R, Witkowski B S et al 2017 *J. Alloys Compd.* **708** 247

[8] Mhamdi A, Saafi I, Hendi A A, Amlouk A, Boubaker K and Amlouk M 2017 *J. Alloys Compd.* **691** 545

[9] Hingorani S, Pillai V, Kumar P, Muntai M S and Shah D O 1993 *Mater. Res. Bull.* **28** 1303

[10] Sakohara S, Ishida M and Anderson M A 1998 *J. Phys. Chem. B* **102** 10169

[11] Zhao X, Zhang S C, Li C, Zheng B and Gu H 1997 *J. Mater. Synth. Process.* **5** 227

[12] Ueda K, Tabata H and Kawai T 2001 *Appl. Phys. Lett.* **79** 988

[13] Venkatesan M, Fitzgerald C B, Lunney J G and Coey J M D 2004 *Phys. Rev. Lett.* **93** 177206

[14] Ozgur U, Alivov Y I, Liu C, Teke A, Reshchikov M A, Dogan S et al 2005 *J. Appl. Phys.* **98** 41301

[15] Jung S W, An S J, Yi G C, Jung C U, Lee S I and Cho S 2007 *Appl. Phys. Lett.* **80** 4561

[16] Lawes G, Risbud A S, Ramirez A P and Seshadri R 2005 *Phys. Rev. B* **71** 45201

[17] Park M S and Min B I 2003 *Phys. Rev. B* **68** 224436

[18] Heo Y W, Ivill M P, Ip K, Norton D P, Pearton S J, Kelly J G et al 2004 *Appl. Phys. Lett.* **84** 2292

[19] Tahir N, Hussain S T, Usman M, Hasanain S K and Mumtaz A 2009 *Appl. Surf. Sci.* **255** 8506

[20] Gupta M K, Lee J H, Lee K Y and Kim S W 2013 *ACS Nano* **7** 8932

[21] Ftouhi H, El-Jouad Z, Jbilou M, Diani M and Addou M 2019 *Eur. Phys. J.: Appl. Phys.* **87** 10301

[22] Kawashima T, Abe D and Washio K 2017 *Mater. Sci. Semicond. Process.* **70** 213

[23] Ghoul J E I 2016 *J. Mater. Sci. Mater. Electron* **27** 2159

[24] Abaira R, Buffagani E, Matoussi A, Khmakhem H and Ferrari C 2015 *Superlattice Microst.* **86** 438

[25] Chang H, Nikolov J, Kim S K, Jang H D, Lim S and Kim D J 2011 *J. Nanosci. Nanotech.* **11** 681

[26] Mallick A and Basak D 2018 *Prog. Mater. Sci.* **96** 86

[27] Roy S, Ghosh M P and Mukherjee S 2021 *Appl. Phys. A* **127** 451

[28] Ghosh M P and Mukherjee S 2019 *J. Am. Ceram. Soc.* **102** 7509

[29] Gupta S, Choubey R K, Sharma K K, Ghosh M P, Kar M and Mukherjee S 2019 *Semicon. Sci. Tech.* **34** 105006

[30] Chen L, Mashimo T, Omurzak E, Okudera H, Iwamoto C and Yoshiasa A 2011 *J. Phys. Chem. C* **115** 9370

[31] Sharma P K, Dutta R K and Pandey A C 2009 *J. Magn. Magn. Mater.* **321** 4001

[32] Morkoc H and Ozgur U 2009 *Zinc oxide—fundamentals, materials and device technology* (1st edn.) (Weinheim: Wiley-VCH Publishers)

[33] Mandal D, Sharma L K and Mukherjee S 2016 *Appl. Phys. A* **122** 1033

[34] Yogamalara R, Srinivasan R, Vinu A, Ariga K and Bose A C 2009 *Solid State Commun.* **149** 1919

[35] Hall W H 1949 *Proc. Phys. Soc. Sect. A* **62** 741

[36] Nath D, Singh F and Das R 2020 *Mater. Chem. Phys.* **239** 122021

[37] Izumi F and Ikeda T 2015 *Annual. Rep. Adv. Ceram. Res.* **3** 33

[38] Biesinger M C, Lau L W M, Gerson A R and Smart R S C 2010 *Appl. Surf. Sci.* **257** 887

[39] Silversmit G, Depla D, Poelman H, Marin G B and Gryse R D 2004 *J. Electron Spectrosc. Relat. Phenomen.* **135** 167

[40] Kennedy J, Murmu P P, Leveneur J, Markwitz A and Futter J 2016 *Appl. Surf. Sci.* **367** 52

[41] Ghosh M P and Mukherjee S 2020 *J. Magn. Magn. Mater.* **498** 166185

[42] Willander M, Nur O, Sadaf J R, Qadir M I, Zaman S, Zainelabdin A et al 2010 *Materials* **3** 2643

[43] Lee M K and Tu H F 2007 *J. Appl. Phys.* **101** 26103

[44] Wei X Q, Man B Y, Liu M, Xue C S, Zhuang H Z and Yang C 2007 *Physica B* **388** 145

[45] Zhao L, Lian J S, Liu Y H, Jiang Q and Nonferr T 2008 *Metal. Soc.* **18** 145

[46] Roro K T, Dangbegnon J K, Sivaraya S, Leitch A W R and Botha J R 2008 *J. Appl. Phys.* **103** 053516

[47] Borseth T M, Svensson B G, Kuznetsov A Y, Klason P, Zhao Q X and Willander M 2006 *Appl. Phys. Lett.* **89** 262112

[48] Cheng W, Wu P, Zou X and Xiao T 2006 *J. Appl. Phys.* **100** 054311

[49] Alaria J, Bouloudenine M, Schmerber G, Colis S, Dinia A, Turek P *et al* 2006 *J. Appl. Phys.* **99** 08M118

[50] Vanheusden K, Seager C H, Warren W L, Tallant D R and Voigt J A 1996 *Appl. Phys. Lett.* **68** 403

[51] Lin B, Fu Z and Jia Y 2001 *Appl. Phys. Lett.* **79** 943

[52] Dijken A V, Meulenkamp E A, Vanmakelbergh D and Meijerink A 2000 *J. Phys. Chem. B* **104** 1715

[53] Zhao Q X, Klason P, Willander M, Zhong H M, Lu W and Yang J H 2005 *Appl. Phys. Lett.* **87** 211912